Monthly Notices
of the
ROYAL ASTRONOMICAL SOCIETY

MNRAS **470,** 932–939 (2017) doi:10.1093/mnras/stx1260
Advance Access publication 2017 May 22

Rapid rotators revisited: absolute dimensions of KOI-13

Ian D. Howarth★ and Giuseppe Morello
Department of Physics and Astronomy, University College London, Gower Street, London WC1E 6BT, UK

Accepted 2017 May 18. Received 2017 May 14; in original form 2017 April 19

ABSTRACT

We analyse *Kepler* light-curves of the exoplanet Kepler Object of Interest no. 13b (KOI-13b) transiting its moderately rapidly rotating (gravity-darkened) parent star. A physical model, with minimal ad hoc free parameters, reproduces the time-averaged light-curve at the ∼10 parts per million level. We demonstrate that this Roche-model solution allows the absolute dimensions of the system to be determined from the star's projected equatorial rotation speed, $v_e \sin i_*$, without any additional assumptions; we find a planetary radius $R_P = (1.33 \pm 0.05)\,R_{♃}$, stellar polar radius $R_{p\star} = (1.55 \pm 0.06)\,R_\odot$, combined mass $M_* + M_P(\simeq M_*) = (1.47 \pm 0.17)\,M_\odot$ and distance $d \simeq (370 \pm 25)$ pc, where the errors are dominated by uncertainties in relative flux contribution of the visual-binary companion KOI-13B. The implied stellar rotation period is within ∼5 per cent of the non-orbital, 25.43-hr signal found in the *Kepler* photometry. We show that the model accurately reproduces independent tomographic observations, and yields an offset between orbital and stellar-rotation angular-momentum vectors of $60\overset{\circ}{.}25 \pm 0\overset{\circ}{.}05$.

Key words: stars: fundamental parameters – stars: individual: KOI-13 – stars: rotation.

1 INTRODUCTION

One of the many unexpected results to emerge from studies of exoplanets this century has been the discovery of orbits that are not even approximately coplanar with the stellar equator (cf., e.g. Winn & Fabrycky 2015).

The tool traditionally most commonly used to investigate the relative orientations of orbital and stellar-rotation angular-momentum vectors is the Rossiter–McLaughlin (R–M) effect (Holt 1893; Schlesinger 1910[1]) – the apparent displacement of rotationally broadened stellar line profiles arising from a body occulting part of the stellar disc. Long established in eclipsing-binary studies (e.g. Rossiter 1924; McLaughlin 1924), the R–M effect took on new significance following its detection in the archetypal transiting exoplanetary system HD 209458 (Queloz et al. 2000). The discovery of misaligned planetary orbits in other systems followed (Hébrard et al. 2008; Winn et al. 2009), and sample sizes are now large enough[2] to suggest that stars with thick convective envelopes generally have planets with small orbital misalignments, while a broader spread of values is found in hotter stars (Schlaufman 2010; Winn et al. 2010; Albrecht et al. 2012; Mazeh et al. 2015).

The R–M effect is an essentially spectroscopic phenomenon, being studied through radial-velocity measurements. In principle, there is a corresponding photometric signature, arising through Doppler boosting (e.g. Groot 2012), but the signal is too small for any reliable detections to date. Transit photometry does, however, offer potential diagnostics of spin-orbit alignment if the surface-brightness distribution over the occulted parts of the stellar disc is not circularly symmetric. In particular, if the stellar rotation is sufficiently rapid, it can introduce both an equatorial extension and, through gravity darkening, a characteristic latitude-dependent surface-intensity distribution; these effects are capable of defining the relative direction of the stellar rotation axis, and hence of diagnosing misaligned transits (e.g. Barnes 2009).

The first system to be recognized as having a misaligned orbit from photometry alone, without supporting evidence from the R–M effect, was Kepler Object of Interest no. 13 (KOI-13; Szabó et al. 2011; Barnes, Linscott & Shporer 2011). Other systems in which asymmetry in the transit light-curve has been interpreted as arising through rotationally induced gravity darkening include KOI-89 (Ahlers, Barnes & Barnes 2015) and HAT-P-7 (KOI-2; Masuda 2015), while the same approach has been used to argue for good alignment of orbital and rotational angular-momentum vectors for KOI-2138 (Barnes et al. 2015). In other cases, modelling of lower-quality data has led to less compelling claims; e.g. PTFO 8-8695 (cp. Barnes et al. 2013; Howarth 2016) and CoRot-29 (cp. Cabrera et al. 2015; Pallé et al. 2016).

In this paper, we re-examine *Kepler* photometry of transits of KOI-13, using a more complete physical model than previous studies. Our intention is to stress-test the model against data of remarkable quality, and to demonstrate its power to establish *absolute* numerical values for key stellar and planetary parameters. Following a selective review of the literature on KOI-13 (Section 2), we summarize the model (Section 3) and the data preparation

★ E-mail: idh@star.ucl.ac.uk

[1] An example of Stigler's law (Merton 1957; Stigler 1980).
[2] ∼120 at the time of writing; e.g. http://www.astro.keele.ac.uk/jkt/tepcat/rossiter.html

(Section 4). Results are presented and discussed in Sections 5 and 6. Appendix A demonstrates how to put the modelling on an absolute scale, given the star's projected equatorial rotation speed.

2 THE KOI-13 SYSTEM

KOI-13 (historically catalogued as BD $+46^\circ$ 2629) was identified as the host of a transiting exoplanet by Borucki et al. (2011). Aitken (1904) had previously noted BD $+46^\circ$ 2629 as a visual binary with components of comparable brightness, separated by $\sim$1.1 arcsec (Howell et al. 2011; Law et al. 2014), which Szabó et al. (2011) showed share a common proper motion. The latter authors identified the marginally brighter component as the transiting system, a result confirmed by Santerne et al. (2012), who found the fainter component, KOI-13B, to be itself a spectroscopic binary.

The basic transit light-curve was modelled by Barnes et al. (2011), who showed that its small asymmetry arises from stellar gravity darkening coupled to spin–orbit misalignment. Subsequent tomography yielded results inconsistent with the obliquity inferred in this first analysis (Johnson et al. 2014), but by imposing the constraint afforded by the spectroscopy, Masuda (2015) was able to identify a geometry that reconciled the spectroscopic and light-curve solutions.

The exquisite quality of the *Kepler* data has inspired a number of ancillary studies. In particular, the system clearly shows out-of-transit orbital variations arising from Doppler beaming, ellipsoidal distortion and reflection effects ('BEER' effects; Shporer et al. 2011; Mazeh et al. 2012; Mislis & Hodgkin 2012). A further, 25.43-hr, periodic signal has been identified in the photometry, and has been suggested as arising either from tidally induced pulsation (Shporer et al. 2011; Mazeh et al. 2012) or from rotational modulation (Szabó et al. 2012).

3 MODELLING

The Barnes et al. (2011) and Masuda (2015) analyses of the transit light-curve were both based on a simple oblate-spheroid stellar geometry and utilized blackbody fluxes coupled to a global two-parameter limb-darkening 'law'. These are reasonable approximations for initial investigations, especially since KOI-13's rotation is substantially subcritical (cf. Table 1), but we undertook our work in the hope that a somewhat more physically based model would better constrain the system with fewer ad hoc adjustments.

The basic model is as described by Howarth (2016; Howarth & Smith 2001). Appropriate values for model parameters, and their probability distributions, are determined through Markov-chain Monte Carlo (MCMC) sampling, with uniform priors unless stated otherwise.

3.1 Star

The star's rotationally distorted surface is approximated as a Roche equipotential.[3] Latitude-dependent values of surface gravity, g, and *local* effective temperature, $T^{\ell}_{\rm eff}$, are calculated self-consistently, taking into account gravity darkening. The stellar flux is then computed as a numerical integration of emitted intensities over visible surface elements.

[3] Mass distributions from polytropic models give negligibly different results (Plavec 1958; Martin 1970). By default, surface angular velocity is assumed to be independent of latitude.

3.1.1 Intensities

Specific intensities (radiances), $I(\lambda, \mu, T^{\ell}_{\rm eff}, g)$, are interpolated from a grid of line-blanketed, solar-abundance local thermodynamic equilibrium models (Howarth 2011a), integrated over the *Kepler* passband. The interpolation in angle ($\mu = \cos\theta$, where θ is the angle between the surface normal and the line of sight) is performed using an analytical four-parameter characterization (Claret 2000)

$$I(\mu)/I(1) = 1 - \sum_{n=1}^{4} a_n(1 - \mu^{n/2}), \tag{1}$$

which reproduces individual numerical values to $\sim$0.1 per cent (Howarth 2011a).

3.1.2 Modelled effective temperature, gravity

Surface distributions of temperature and gravity are needed in order to evaluate model-atmosphere emergent intensities (and for no other reason). These parameters are completely specified by the adopted gravity-darkening law (Section 3.1.3), plus any suitable normalizations; we use the base-10 logarithm of the polar gravity in c.g.s. units, $\log g_{\rm p}$, and the stellar effective temperature,

$$T_{\rm eff} = \sqrt[4]{\frac{\int \sigma (T^{\ell}_{\rm eff})^4 \, {\rm d}A}{\int \sigma \, {\rm d}A}}$$

(where σ is the Stefan–Boltzmann constant and the integrations are over surface area).

While the use of model-atmosphere intensities removes the need for ad hoc limb-darkening parameters, this is at the expense of assumptions that, first, the effective temperature and polar gravity are known with adequate precision to give a sufficiently faithful representation of limb darkening, and secondly, that the model-atmosphere calculations predict the emergent intensities reliably. Anticipating that neither assumption needs necessarily be valid (e.g. Howarth 2011b), we draw an explicit distinction between the actual physical quantities $T_{\rm eff}$, $\log g_{\rm p}$ and their model-parameter counterparts $T^{\rm L}_{\rm eff}$, $\log g^{\rm L}_{\rm p}$ (where the superscript is intended to indicate a 'light-curve', or 'limb-darkening', determination; cf. Section 5).

3.1.3 Gravity darkening

It is not immediately obvious whether gravity darkening in KOI-13 should be modelled according to a recipe appropriate for radiative or convective envelopes. While the literature documents a surprising large dispersion for estimates of its effective temperature (7650–9107 K; Brown et al. 2011, Szabó et al. 2011, Huber et al. 2014, Shporer et al. 2014, with claimed precisions that are considerably smaller than the spread of results), the more detailed studies tend towards values at the lower end of the range. This puts $T_{\rm eff}$ not very far from the boundary between convective and radiative regimes, around $T_{\rm eff} \simeq 7000$ K (e.g. Claret 1998). Because of this, we ran several sequences of models using a generic gravity-darkening law,

$$T^{\ell}_{\rm eff} \propto g^{\beta}, \tag{2}$$

with the gravity-darkening exponent β as a free parameter. These models all migrated to solutions with exponents very close to the von Zeipel (1924) value of $\beta = 0.25$, as was also found by Masuda (2015).

For most model runs, we actually used the parameter-free gravity-darkening model proposed by Espinosa Lara & Rieutord (2011),

Table 1. Model parameters and illustrative fitted values. Model M1 has $T^{\mathrm{L}}_{\mathrm{eff}}$ as a free parameter (cf. Section 3.1.2), with $\log g^{\mathrm{L}}_{\mathrm{p}} \equiv \log g_{\mathrm{p}}$; model M2 additionally has $\log g^{\mathrm{L}}_{\mathrm{p}}$ free; model M3 has P_{rot} fixed. The errors (on the last quoted significant figure of the parameter values) are the quadratic sum of 95-percentile ranges on solution M1 (initial $L_3 = 0.45$) and the maximum deviation of corresponding solutions with initial L_3 values in the range 0.41–0.49 (Section 5.2).

	Parameter	Best-fitting value			
	Model:	M1	±	M2	M3
Stellar:					
$T^{\mathrm{L}}_{\mathrm{eff}}$	Effective-temperature parameter[a] (K)	8084	186	7987	8046
$\log g^{\mathrm{L}}_{\mathrm{p}}$	Polar-gravity parameter[a] (dex cgs)	–		4.27	4.32
$\Omega/\Omega_{\mathrm{c}}$	Angular rotation rate (in units of the critical rate)	0.341	15	0.343	0.320
i_*	Inclination of stellar rotation axis to line of sight (0–90°)	81.137	16	81.135	81.134
$R_{\mathrm{p}\star}/a$	Polar radius (in units of the orbital semi-major axis)	0.2219	4	0.2217	0.2219
L_3	'Third light'	0.451	39	0.451	0.451
g.d.	Gravity darkening: ELR				
Planetary:					
R_{P}/a	Planetary radius(in units of the orbital semi-major axis)	0.0190	7	0.0190	0.0190
Orbital:					
i_{orb}	Inclination of orbital angular-momentum vector to line of sight (0–180°)	93.319	22	93.316	93.316
λ	Angle between the projections on to the plane of the sky of the orbital and stellar-rotational angular-momentum vectors, measured counter-clockwise from the former (0–360°)	59.19	5	59.20	59.20
Imposed:					
P_{orb}	Orbital period (d)	1.76358799			
$v_{\mathrm{e}} \sin i_*$	Projected equatorial rotation speed[b] (km s^{-1})	76.6 ± 0.2			
P_{rot}	Rotation period (d)	–		–	1.0596
Derived stellar parameters:					
$\log g_{\mathrm{p}}$	True polar gravity (dex cgs)	4.209	19	4.21	4.24
$R_{\mathrm{p}\star}/\mathrm{R}_{\odot}$	Polar radius	1.49	7	1.48	1.61
$R_{\mathrm{e}}/\mathrm{R}_{\odot}$	Equatorial radius	1.52	7	1.51	1.63
Oblateness	$1 - R_{\mathrm{p}\star}/R_{\mathrm{e}}$	0.0178	17	0.0181	0.0156
$T_{\mathrm{p}}/T_{\mathrm{eff}}$	Relative polar temperature	1.0118	11	1.0119	1.0103
$T_{\mathrm{e}}/T_{\mathrm{eff}}$	Relative equatorial temperature	0.9939	6	0.9938	0.9947
$(1+q)M_*/\mathrm{M}_{\odot}$	System mass[c]	1.31	17	1.29	1.64
$\log(L^{\mathrm{L}}/\mathrm{L}_{\odot})$	luminosity $\times (T_{\mathrm{eff}}/T^{\mathrm{L}}_{\mathrm{eff}})^4$ (dex solar)	0.94	3	0.92	1.00
ρ_*	Mean density (g cm^{-3})	0.5373	11	0.5380	0.5397
v_{e}	Equatorial rotation speed (km s^{-1})	77.3	4	77.5	78.0
P_{rot}	Rotation period (d)	0.994	23	0.987	–
Other derived parameters:					
$R_{\mathrm{P}}/\mathrm{R}_{♃}$	Planetary radius ($\mathrm{R}_{♃} = (\mathcal{R}^{\mathrm{N}}_{e\mathrm{J}}\mathcal{R}^{\mathrm{N}}_{p\mathrm{J}})^{1/2}$)	1.28	5	1.28	1.38
ψ	Angle between orbital and stellar-rotational angular-momentum vectors (0–180°)	60.24	5	60.25	60.25
b	Impact parameter ($R_{\mathrm{p}\star}$)	0.2609	12	0.2609	0.2607

Notes. Additional model parameters include e, the orbital eccentricity ($e = 0$ assumed here) and longitude of periastron (0–360°; undefined when $e = 0$). Best-fit (minimum-χ^2) parameter sets are listed; median values of MCMC runs are extremely close to these values.
[a]Used only to evaluate model-atmosphere intensities, and constrained in the present study only by limb darkening; cf. Section 5.1
[b]Derived radii scale linearly with $v_{\mathrm{e}} \sin i_*$, and the mass as $(v_{\mathrm{e}} \sin i_*)^3$; Appendix A.
[c]Mass ratio $q \equiv M_{\mathrm{P}}/M_* \simeq 4 \times 10^{-3}$ (Shporer et al. 2014; Esteves et al. 2015; Faigler & Mazeh 2015).

which is close to von Zeipel gravity darkening at the subcritical rotation appropriate to KOI-13. This 'ELR' formulation has a somewhat firmer physical foundation than the original von Zeipel analysis, and gives better agreement with, in particular, optical interferometry of rapid rotators (e.g. Domiciano de Souza et al. 2014).

3.2 Transit

Transits are modelled by assuming a completely dark occulting body of circular cross-section, in a misaligned circular orbit; although an orbital eccentricity $e = (6 \pm 1) \times 10^{-4}$ has been inferred from out-of-transit photometry of KOI-13 by Esteves, De Mooij & Jayawardhana (2015), this has negligible consequences for our study. The contamination of the transit light-curve by KOI-13B (spatially unresolved in the *Kepler* beam) is characterized by its fractional contribution to the total signal, or 'third light' (L_3) in the nomenclature of traditional eclipsing-binary studies.[4]

3.3 Parameters

Table 1 lists one set of basic parameters that fully specify the model (other combinations are possible). We stress that the geometry of the model is fundamentally scale-free; all linear dimensions are expressed in units of the orbital semi-major axis, while times are implicitly in units of the orbital period. The extent of effects arising from rotational distortion is determined by $\Omega/\Omega_{\mathrm{c}}$, the ratio of the rotational angular velocity to the critical value at which the effective

[4] Of course, the exoplanetary 'second light' is extremely small.

equatorial gravity is zero; a value for the stellar mass, often assumed in similar studies, is not required.

4 DATA PREPARATION

We used the full set of short-cadence Pre-search Data Conditioning Simple Aperture Photometry (PDCSAP) data, which are publicly available through the *Kepler* Input Catalogue (Brown et al. 2011). The PDCSAP results are produced by the standard *Kepler* pipeline, which removes instrumental artefacts, and span from 2009 June to 2013 May.

The sampling step of 58.9 s corresponds to $\sim 4 \times 10^{-4}$ of the 1.7-d orbital period. The maximum difference between 'instantaneous' and exposure-integrated model fluxes in the parameter space of interest is 6 parts per million (ppm), which is small enough to be neglected (deviations exceed 1 ppm for a phase range of <0.001).

The system shows out-of-transit orbital variations arising from BEER effects (Section 2). Even over the limited phase range that we model, $\pm 0.1 P_{\rm orb}$ around conjunction, the amplitude of these effects is ∼40 ppm, which is far from negligible. We treated these effects as a perturbation on the basic model, and corrected for them by using the empirical three-harmonics model[5] described by Shporer et al. (2014).

The 25.43-hr signal has a semi-amplitude variously reported as 12–30 ppm (Shporer et al. 2011; Mazeh et al. 2012; Szabó et al. 2012); from the limited out-of-transit phase range of our data, we determine a semi-amplitude of only 6 ppm, suggesting that the amplitude may be variable. Although the period is close to a 3:5 resonance with the orbital period (Shporer et al. 2011), the ratio is not exact. Consequently, this signal is 'mixed out' over the ∼4-yr span of the observations when phased on transits, and effectively becomes only a minor source of additional stochastic noise.

In order to reduce the 299 423 individual observations down to a manageable subset for MCMC modelling, for each of 577 separate transits the data were first phased (according to the ephemeris used in the current MCMC cycle), corrected for BEER effects, and rescaled to give a median out-of-transit flux of one.[6] In principle, any free parameters in the adopted functional form for the ephemeris could be allowed to 'float' in the fitting process; in practice, we adopted a linear ephemeris with a fixed period ($P_{\rm orb} = 1.763\,587\,99$ d; Shporer et al. 2014), but allowed the time of conjunction to vary.

We then compressed the resulting data by taking median normalized fluxes in phase bins of 0.0002 (about half the integration time of individual observations), whence each bin contained ∼300 data points. The maximum change in normalized flux between the central times of bins is 1.2×10^{-4}, which is comparable to the dispersion of the individual data points ($\sim 1.6 \times 10^{-4}$ out of transit), but large compared to the precision of the binned data ($\sim 1.0 \times 10^{-5}$); consequently, we tagged the median flux in each bin with the mean time of all observations in that bin (invariably close to the mid-bin time) rather than its original, individual phase.

5 FIT RESULTS

As a basis for subsequent discussion, we first present the results of an initial 'maximally constrained' model, in which only (effectively) geometric parameters were adjusted. ELR gravity darkening (Espinosa Lara & Rieutord 2011) and model-atmosphere limb-darkening were used, along with fixed values for $T_{\rm eff}$ (7650 K; Shporer et al. 2014) and L_3 (0.45; Szabó et al. 2011). The results of this 'model 0' are illustrated in Fig. 1 and show relatively large residuals during ingress and egress (∼50 ppm).

We investigated the origin of these residuals through extensive exploration of model parameters. Adopting equation (2) with β free essentially reproduced von Zeipel's law, which, in turn, gives sensibly identical results to the ELR model (unsurprisingly, since the latter is known to reproduce von Zeipel at low to moderate rotation). Moderate adjustments to L_3 had similarly small consequences for

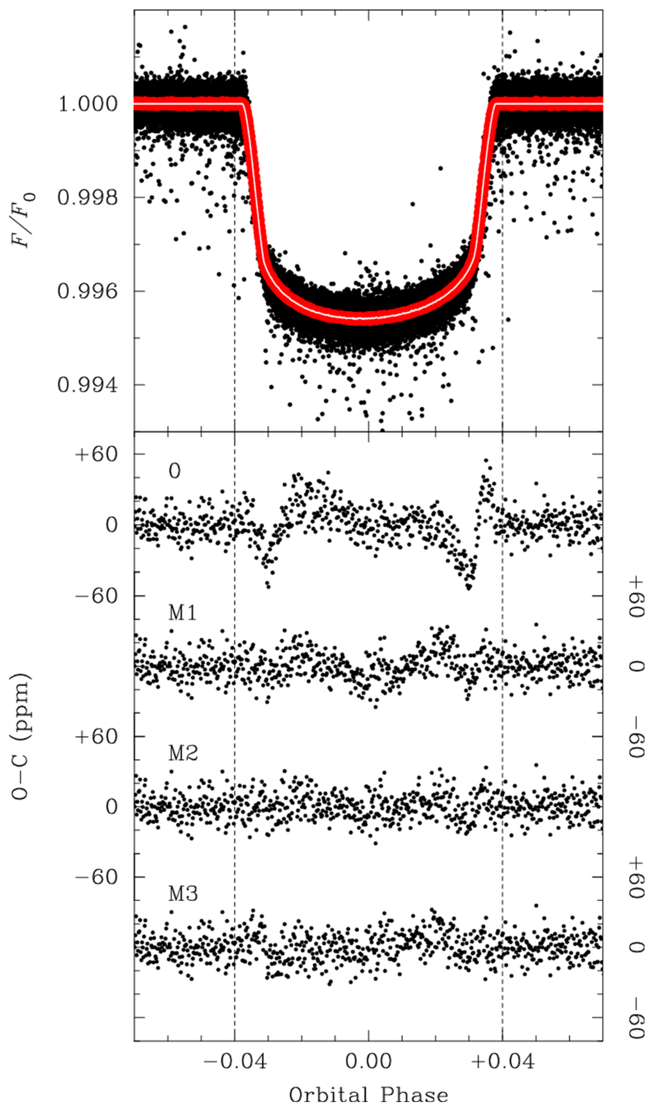

Figure 1. Phase-folded *Kepler* photometry. In the top panel, the small black dots represent individual observations, and large red dots (which blend into a continuous band) are the median values in phase bins of 0.002. The white line through the medians is from model M2 (Section 5); any other gravity-darkened model is virtually indistinguishable at the scale of this plot. The lower panel shows O−C residuals for different models (cf. Section 5). Model 0 is for $T_{\rm eff} = 7650$ K, $L_3 = 0.45$; model M1 is as model 0 but with $T^{\rm L}_{\rm eff}$ free; model M2 is as model M1, but with $\log g^{\rm L}_{\rm p}$ also free; model M3 is as model M2, but with the rotation period fixed. Vertical dashed lines are intended simply as a visual aid to identifying transit phases.

[5] The model defined by eqtnion (11) and table 5 of Shporer et al. has to be reversed in both x and y.

[6] 'Out of transit' was taken as $0.045 \leq |\phi| \leq 0.1$, where orbital phase ϕ is measured in the range −0.5: +0.5 about conjunction.

the quality of the model fits. These experiments identified errors in the limb darkening as the principal cause of the discrepancies.

We addressed this issue in three ways. First, we replaced the near-exact representation of the angular dependence of the model-atmosphere intensities afforded by equation (1) with a simple quadratic limb-darkening law,

$$I(\mu)/I(1) = 1 - u_1(1-\mu) - u_2(1-\mu)^2, \quad (3)$$

with the coefficients u_1, u_2 as free parameters. In applying this law globally (in common with, e.g. Masuda 2015), we abandon any latitudinal temperature dependence of the coefficients.

Secondly, in a gesture towards retaining temperature-dependent limb-darkening while introducing only a single additional free parameter, we investigated scaling the linear (a_2) term in the four-coefficient characterization.[7]

Thirdly, recognizing that there is a temperature dependence of the model limb darkening, we allowed the effective-temperature parameter to float; that is, we characterize the model-atmosphere intensities by $T^{\rm L}_{\rm eff}$ rather than $T_{\rm eff}$ (Section 3.1.2).

Unsurprisingly, all three approaches gave improved model fits, but it is noteworthy that quite small adjustments to the model effective temperature have significant consequences at the ∼10 ppm level of precision, solely through the modest sensitivity of $I(\mu)/I(1)$ to this parameter. In practice, allowing $T^{\rm L}_{\rm eff}$ to float also led to smaller residuals than the other approaches in our numerical experiments; we adopt the corresponding results for this reason, and to avoid introducing additional ad hoc parameters. Numerical values for this 'model M1' are included in Table 1, and it is confronted with the observations in Fig. 1. Fig. 2 is a simple cartoon illustrating the implied geometry of the system.

Model-atmosphere intensities are a function of not only temperature, but also surface gravity (as well as abundances and microturbulence). The true polar gravity, $\log g_{\rm p}$ (which, with $\Omega/\Omega_{\rm c}$, characterizes the overall surface-gravity distribution) is not a free parameter in our model (Section 6). However, we can allow the value used in obtaining the model-atmosphere intensities, $\log g^{\rm L}_{\rm p}$, to 'float' as, effectively, an additional limb-darkening parameter. Doing this naturally affords further, albeit slight, improvement in the model fit (model M2 in Table 1 and Fig. 1).

The remaining systematic residuals (peaking at <10 ppm) may arise from orbital evolution over the duration of the *Kepler* observations (Szabó et al. 2012; Szabó, Simon & Kiss 2014; Masuda 2015), since the time-averaged light-curve will not correspond to any single-epoch photometry. Modelling the time-dependent behaviour is beyond the scope of this paper, partly because of the substantial computing requirements required to model necessarily less compacted data sets (we may return to this in future work), but also because our discussion of third light (Section 5.2) emphasizes that the uncertainties on fundamental parameters (our main interest here) are likely to be dominated by other factors.

5.1 Effective temperature and limb darkening

We recall that the effective-temperature 'determination' in the model is not a traditional, direct measurement of the actual stellar effective temperature, $T_{\rm eff}$; rather, $T^{\rm L}_{\rm eff}$ is simply a parameter that optimizes model-atmosphere limb darkening (over the *range* of surface temperatures) to give a best match to the transit data.[8] Only if the calculated model-atmosphere intensities are sufficiently accurate will $T^{\rm L}_{\rm eff}$ correspond to the actual effective temperature.

However, it is noteworthy that, in practice, the optimized value of $T^{\rm L}_{\rm eff}$ falls well within the range of direct $T_{\rm eff}$ determinations; while adopting only a moderately different fixed value gives relatively large residuals. This highlights the importance of establishing the correct value of $T_{\rm eff}$ when comparing empirical and theoretical limb-darkening coefficients (or when adopting the latter). Fig. 3 shows the limb darkening for a model atmosphere at $T_{\rm eff}$ = 8.00 kK, $\log g$ = 4.2, representative of the parameter space within which our solutions fall. The maximum difference in normalized intensity, $I(\mu)/I(1)$, between this model and one at 7.65 kK is less than 2 per cent, and yet this difference accounts for almost all of the residuals for Model 0 shown in Fig. 1.

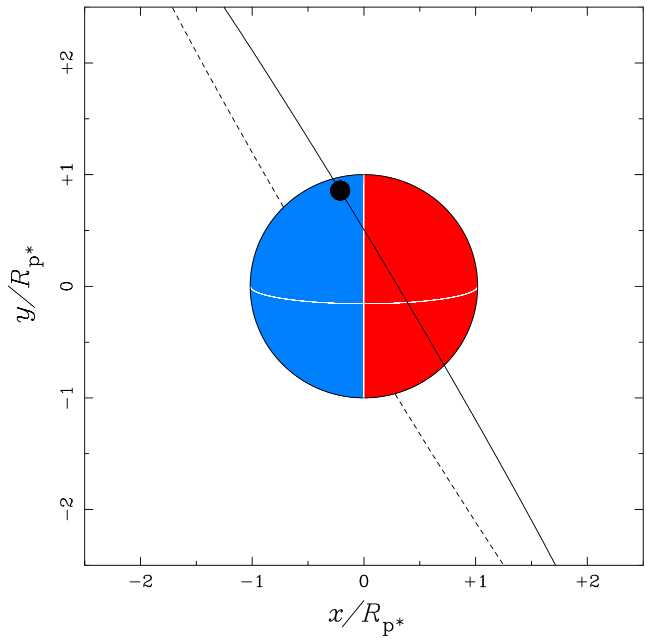

Figure 2. Cartoon view of the system. The origin of the co-ordinates is the stellar centre of mass, and the projected stellar-rotation axis is arbitrarily orientated along the y axis; the exoplanet orbit extends to $a \simeq 4.5R_{\rm p\star}$. The approaching and receding stellar hemispheres are colour-coded blue and red (in the on-line version); note that the star is *slightly* oblate. The exoplanet is shown at orbital phase −0.03 (thereby indicating the direction of orbital motion). The model is degenerate with its mirror image about the y axis.

5.2 Third light

The third light of the unresolved optical companion KOI-13B is (literally) a nuisance parameter in our modelling. For our MCMC runs, we experimented with initial values of L_3 = 0.41–0.49 ($\Delta m \simeq$ 0.40–0.04), which bracket most observational determinations in the literature[9] (Fabricius et al. 2002; Adams et al. 2012; Law et al. 2014; Shporer et al. 2014), at steps of 0.02.

[7] There is a minor inconsistency in both the first and second approaches, in that the integral of intensity over angle will, in general, no longer *exactly* match the model-atmosphere flux, but this is unimportant for our application.

[8] The same caveat applies to $\log g^{\rm L}_{\rm p}$; the actual value of $\log g_{\rm p}$ is fixed by other model parameters (Section 6).

[9] Howell et al. (2011) report notably discordant values of $\Delta m \simeq$ 0.8–1.1 at ∼600–700 nm. Although the literature values are for diverse wavebands, the KOI-13A and B components are of similar spectral types and colours (Szabó et al. 2011), so any wavelength dependence of L_3 should be small in the optical regime.

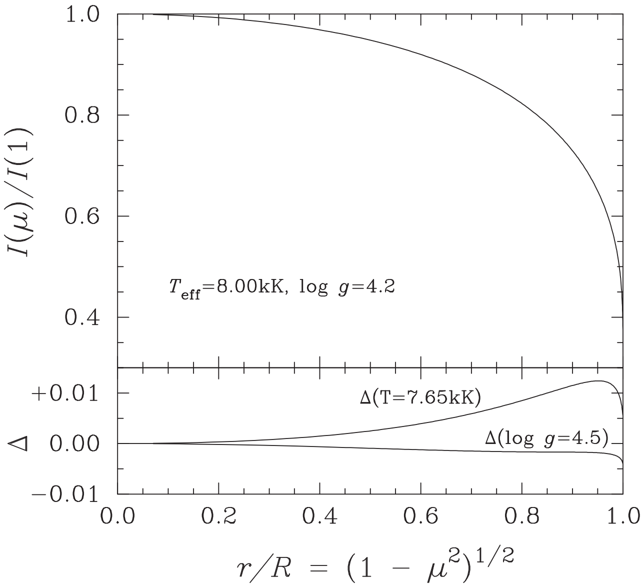

Figure 3. Upper panel: normalized model-atmosphere limb darkening at $T_{\rm eff} = 8.0$ kK, $\log g = 4.2$, close to values for our best-fitting models (which take into account the latitude dependence of these parameters). Lower panel: differences in limb darkening for adjusted values, as indicated (in the sense reference minus adjusted; note the 10-fold change in y-axis scale).

We found that the adopted third light always clung very close to the initial estimate in our MCMC modelling, rather than converging on to a value representing the global minimum in χ^2 hyperspace. This contrasts with the behaviour of other parameters, whose values freely migrated over relatively large ranges during 'burn-in'. Adjusting the proposal distribution did not alleviate this issue.

We believe that this outcome may arise because the transit light-curve contains almost no information on the extent of third-light dilution (cf., e.g. fig. 8 of Seager & Mallén-Ornelas 2003). Although we might anticipate that this should be reflected in a *wide* distribution in acceptable L_3 values, rather than a narrow one, in practice the set of other parameters essentially locks in L_3, which can therefore be regarded, in a limited sense, as a 'derived' parameter, given the system geometry, rather than a free one.

The inferred numerical values for other parameters therefore depend somewhat on L_3, to a degree that typically exceeds the formal errors on any given model. For example, smaller L_3 means a shallower true transit depth, and hence implies smaller $R_{\rm P}/R_*$ ($\Delta(R_{\rm P}/R_*) \simeq 0.08\Delta L_3$). In recognition of this, while we adopt solutions with input $L_3 = 0.45$ (which yield the smallest residuals), we give errors in Table 1, which are the quadratic sum of the 95 per cent-percentile ranges on those models and the maximum differences with the 'best-fitting' parameters from models with L_3(init.) = 0.41–0.49 (where the latter term dominates).

5.3 Rotation period

Our initial solutions (e.g. models M1 and M2) yielded rotation periods close to 24 hr, only ~5 per cent from the 25.43-hr period found in the *Kepler* photometry (Shporer et al. 2011; Mazeh et al. 2012; Szabó et al. 2012). Although rotational modulation had not been widely anticipated for stars hotter than the 'granulation boundary' marking the transition from radiative to convective envelopes (e.g. Gray & Nagel 1989), evidence is beginning to accumulate for starspots, of some nature, in A-type stars (Balona 2011, 2017; Böhm et al. 2015), encouraging consideration of the possibility that we are seeing a rotational signature in KOI-13 ($T_{\rm eff} \simeq 8$ kK corresponds to spectral type A5–A7), as suggested by Szabó et al. (2012).

We can impose the constraint of fixed $P_{\rm rot}$ on the model, which links $\Omega/\Omega_{\rm c}$ to $R_{\rm p\star}/a$ in the MCMC chains (Appendix A, equation A2). The results of this model M3 are reported in Table 1; the fit quality is quite reasonable (Fig. 1). Because the transit depth essentially fixes $R_{\rm P}/R_*$, the main effect of imposing a longer rotation period is to decrease the angular rotation rate, which for given $v_{\rm e} \sin i_*$ leads to a larger stellar radius, and hence, for ~fixed density, a higher stellar mass, as discussed in the Section 6.

5.4 Tomography

There are no published Rossiter–McLaughlin investigations of KOI-13, but Johnson et al. (2014) conducted a detailed tomographic study, providing a velocity-resolved map of the transit.

Our model allows stellar velocities (R–M effect or tomographic counterpart) to be evaluated directly. This can be accomplished by synthesizing the spectrum as a function of orbital phase, and subjecting the ensemble of synthetic spectra to the same analysis as the observations (e.g. cross-correlation, or tomography). However, for this study, we simply take the intensity-weighted average radial velocity,

$$v(\lambda) = \frac{\int v \times I(\lambda, \mu, T^{\ell}_{\rm eff}, g)\, {\rm d}A}{\int I(\lambda, \mu, T^{\ell}_{\rm eff}, g)\, {\rm d}A},$$

where the integration is over area, and the (weak) wavelength dependence of the model velocity comes about because of the wavelength dependence of intensities on limb darkening and temperature. To evaluate the R–M effect, the integration is conducted over all visible elements, while taking the velocity of all occulted elements models the tomographic signature.

The predicted locus of velocity versus phase from the light-curve solution is compared to the Johnson et al. map in Fig. 4. The agreement is very satisfactory, arising from the accord between the values of projected obliquity λ and impact parameter b obtained from the *independent* tomographic and photometric solutions ($\Delta\lambda = 0\overset{\circ}{.}6 \pm 2\overset{\circ}{.}0$, $\Delta b = 0.01 \pm 0.03$).

6 SYSTEM PARAMETERS

Any fundamentally geometric transit model, such as employed here, is of necessity scale-free. Consider Fig. 2; there is no indication of whether this is a small, nearby system or a large, distant one.

Nevertheless, for given orbital period, a large, distant system must have greater orbital velocities, and hence greater masses, than a smaller, nearby system. This relationship between scale and mass is codified in Kepler's third law, which leads directly to a constraint on $a^3/(M_* + M_{\rm P})$, and hence, given the dimensionless radius R_*/a, to the stellar density (e.g. Seager & Mallén-Ornelas 2003) – but not the mass and radius separately.

Barnes et al. (2011) suggested that rotational effects, and specifically gravity darkening, can, in principle, lift the 'density degeneracy', through the dependence of Ω on mean stellar radius R_*. However, in the Roche approximation the light-curve depends on rotational effects only through the ratio $\Omega/\Omega_{\rm c}$; to get to Ω requires calculation of $\Omega_{\rm c}$, which itself has an M/R^3 dependence. Consequently, Ω is actually scale-free (as shown analytically in Appendix A), and a Roche-model analysis of the transit light-curve alone cannot break the mass/radius degeneracy in M/R^3.

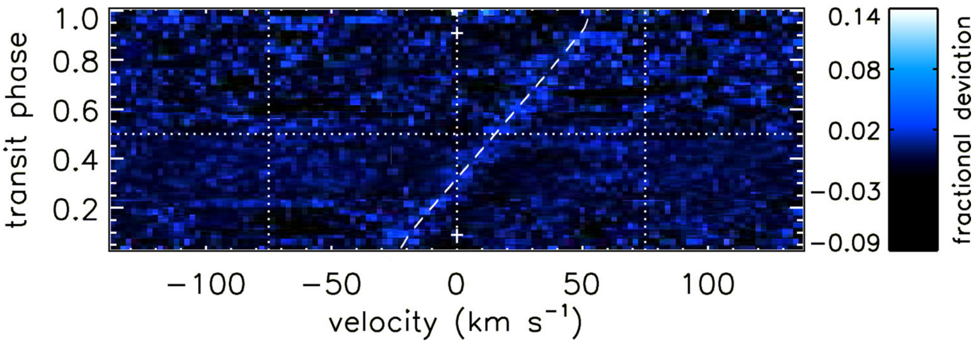

Figure 4. Tomographic transit map, from Johnson et al. (2014, slightly contrast enhanced), overlaid with the prediction of the light-curve model (dashed line). To make the comparison, we assume that the Johnson et al. 'transit phase' runs from first to fourth contact, and adopt their value of 76.6 km s^{-1} for $v_e \sin i_*$ (which directly determines the *x*-axis scaling).

Of course, if the orbital velocities can be established for both components, these determine the absolute scale – the standard 'double-lined eclipsing binary' approach. However, an alternative, independent means of establishing the orbital semi-major axis (and hence other system parameters) is available if $P_{\rm rot}$, the stellar rotation period, i_*, the axial inclination, and $v_e \sin i_*$, the line-of-sight component of the equatorial rotation speed, can be determined; these immediately yields the equatorial radius,

$$R_e = (P_{\rm rot} v_e \sin i_*)/(2\pi \sin i).$$

The quantities $P_{\rm rot}$ and i_* can be estimated if the circular symmetry of the projected stellar disc is broken. A familiar example is when starspots are present, but gravity-darkened stars have the same potential (since Ω/Ω_c relates, indirectly, to $P_{\rm rot}$). Introducing the observed projected equatorial rotation speed, $v_e \sin i_*$, as a constraint on the light-curve solution therefore affords usefully tight limits on the absolute dimensions of the system. The straightforward algebra is set out in Appendix A.

There are two precise determinations of projected rotation speed of KOI-13A in the literature, in good mutual agreement: $v_e \sin i_* = 76.96 \pm 0.61$ and 76.6 ± 0.2 km s^{-1} (Santerne et al. 2012; Johnson et al. 2014). We adopt the latter, more precise value in order to calculate the system dimensions reported in Table 1.

[Our referee raised the point that the precision of these results may not reflect their accuracy, an observation with which we fully concur (cf., e.g. Howarth 2004). However, as shown in Appendix A (equation A2), the semi-major axis scales linearly with $v_e \sin i_*$; radii converted from normalized to absolute values scale in the same way, while the absolute system mass scales as $(v_e \sin i_*)^3$, from Kepler's third law. Hence, the results, or uncertainties, are readily reassessed if another value for the projected equatorial rotation speed is preferred.]

6.1 Distance

The effective temperature determines the surface brightness; given the size of the star, the absolute magnitude follows, and hence the distance. We find

$$M(V) \simeq 2.44 + 0.51\left(8.0 - \frac{T_{\rm eff}}{\rm kK}\right) - 5\log\left(\frac{R_{\rm p*}}{1.49{\rm R}_\odot}\right),$$

where the second term is an empirical fit to models with $7.5 < T_{\rm eff}/{\rm kK} < 8.5$; model-atmosphere Johnson *V*-band fluxes are from Howarth (2011a); and we neglect the further, unimportant, dependences of $M(V)$ on Ω/Ω_c and i_*.

There is a surprisingly large dispersion in the photometry of KOI-13 catalogued in the *Vizier* system of the Centre de Données astronomiques de Strasbourg, most of which clearly refers to the combined light of the visual binary. We adopt the spatially resolved Tycho-2 photometry, which transforms to $V = 10.33$ for KOI-13A (with an uncertainty of ∼0.05; Høg et al. 2000). Foreground reddening is estimated as $E(B - V) \simeq 0\overset{\rm m}{.}02$ from Green et al. (2015), whence

$$\log\left(\frac{d}{\rm pc}\right) = 2.566 + 0.2\,[(V - 10.33) - (A(V) - 0.06)] \\ -0.102\left(8.0 - \frac{T_{\rm eff}}{\rm kK}\right) + \log\left(\frac{R_{\rm p*}}{1.49{\rm R}_\odot}\right);$$

i.e. $d \simeq 370$ pc, with an uncertainty of perhaps ∼25 pc.

7 CONCLUSIONS

We have conducted a new solution of *Kepler* photometry of transits of KOI-13b, obtaining results that are substantially in agreement with those found by Masuda (2015), and in accord with the tomography reported by Johnson et al. (2014). The solution yields both the projected and true angular separations of the orbital and stellar-rotation angular-momentum vectors. We emphasize that any photometric solution is necessarily scale-free (e.g. does not require a stellar mass to be assumed); but demonstrate that, by adopting a value for $v_e \sin i_*$, the absolute system dimensions and mass can be established. Allowing for the full range of solutions (Table 1; third light $L_3 = 0.41$–0.49, free or fixed stellar rotation period), we obtain a planetary radius $R_{\rm P}/{\rm R}_{♃} = 1.33 \pm 0.05$, stellar polar radius $R_{\rm p\star}/{\rm R}_\odot = 1.55 \pm 0.06$ and a combined mass $M_* + M_{\rm P} (\simeq M_*) = 1.47 \pm 0.17\ {\rm M}_\odot$. All solutions place KOI-13 in an unremarkable location in the main-sequence mass–radius plane (e.g. Eker et al. 2015).

REFERENCES

Adams E. R., Ciardi D. R., Dupree A. K., Gautier III T. N., Kulesa C., McCarthy D., 2012, AJ, 144, 42
Ahlers J. P., Barnes J. W., Barnes R., 2015, ApJ, 814, 67
Aitken R. G., 1904, Lick Obs. Bull., 3, 6
Albrecht S. et al., 2012, ApJ, 757, 18
Balona L. A., 2011, MNRAS, 415, 1691
Balona L. A., 2017, MNRAS, 467, 1830
Barnes J. W., 2009, ApJ, 705, 683
Barnes J. W., Linscott E., Shporer A., 2011, ApJS, 197, 10

Barnes J. W., van Eyken J. C., Jackson B. K., Ciardi D. R., Fortney J. J., 2013, ApJ, 774, 53
Barnes J. W., Ahlers J. P., Seubert S. A., Relles H. M., 2015, ApJ, 808, L38
Böhm T. et al., 2015, A&A, 577, A64
Borucki W. J. et al., 2011, ApJ, 736, 19
Brown T. M., Latham D. W., Everett M. E., Esquerdo G. A., 2011, AJ, 142, 112
Cabrera J. et al., 2015, A&A, 579, A36
Claret A., 1998, A&AS, 131, 395
Claret A., 2000, A&A, 363, 1081
Domiciano de Souza A. et al., 2014, A&A, 569, A10
Eker Z. et al., 2015, AJ, 149, 131
Espinosa Lara F., Rieutord M., 2011, A&A, 533, A43
Esteves L. J., De Mooij E. J. W., Jayawardhana R., 2015, ApJ, 804, 150
Fabricius C., Høg E., Makarov V. V., Mason B. D., Wycoff G. L., Urban S. E., 2002, A&A, 384, 180
Faigler S., Mazeh T., 2015, ApJ, 800, 73
Gray D. F., Nagel T., 1989, ApJ, 341, 421
Green G. M. et al., 2015, ApJ, 810, 25
Groot P. J., 2012, ApJ, 745, 55
Harrington J. P., Collins II G. W., 1968, ApJ, 151, 1051
Hébrard G. et al., 2008, A&A, 488, 763
Holt J. R., 1893, A&A, 12, 646
Howarth I. D., 2004, in Maeder A., Eenens P., eds, IAU Symp. 215, Stellar Rotation. Kluwer, Dordrecht, p. 33
Howarth I. D., 2011a, MNRAS, 413, 1515
Howarth I. D., 2011b, MNRAS, 418, 1165
Howarth I. D., 2016, MNRAS, 457, 3769
Howarth I. D., Smith K. C., 2001, MNRAS, 327, 353
Howell S. B., Everett M. E., Sherry W., Horch E., Ciardi D. R., 2011, AJ, 142, 19
Huber D. et al., 2014, ApJS, 211, 2
Høg E. et al., 2000, A&A, 355, L27
Johnson M. C., Cochran W. D., Albrecht S., Dodson-Robinson S. E., Winn J. N., Gullikson K., 2014, ApJ, 790, 30
Law N. M. et al., 2014, ApJ, 791, 35
Martin P. G., 1970, Ap&SS, 7, 119
Masuda K., 2015, ApJ, 805, 28
Mazeh T., Nachmani G., Sokol G., Faigler S., Zucker S., 2012, A&A, 541, A56
Mazeh T., Perets H. B., McQuillan A., Goldstein E. S., 2015, ApJ, 801, 3
McLaughlin D. B., 1924, ApJ, 60
Merton R. K., 1957, Am. Sociological Rev., 22, 635
Mislis D., Hodgkin S., 2012, MNRAS, 422, 1512
Pallé E. et al., 2016, A&A, 589, A62
Plavec M., 1958, Mem. Soc. R. Sci. Liège, 20, 411
Queloz D., Eggenberger A., Mayor M., Perrier C., Beuzit J. L., Naef D., Sivan J. P., Udry S., 2000, A&A, 359, L13
Rossiter R. A., 1924, ApJ, 60
Santerne A. et al., 2012, A&A, 544, L12
Schlaufman K. C., 2010, ApJ, 719, 602
Schlesinger F., 1910, Publ. Allegheny Obs. Univ. Pittsburgh, 1, 123
Seager S., Mallén-Ornelas G., 2003, ApJ, 585, 1038
Shporer A. et al., 2011, AJ, 142, 195
Shporer A. et al., 2014, ApJ, 788, 92
Stigler S. M., 1980, Trans. New York Acad. Sci., 39, 147
Szabó G. M. et al., 2011, ApJ, 736, L4
Szabó G. M., Pál A., Derekas A., Simon A. E., Szalai T., Kiss L. L., 2012, MNRAS, 421, L122
Szabó G. M., Simon A., Kiss L. L., 2014, MNRAS, 437, 1045
von Zeipel H., 1924, MNRAS, 84, 665
Winn J. N., Fabrycky D. C., 2015, ARA&A, 53, 409
Winn J. N. et al., 2009, ApJ, 700, 302
Winn J. N., Fabrycky D., Albrecht S., Johnson J. A., 2010, ApJ, 718, L145

APPENDIX A: SCALING

The photometric solution establishes reasonably precise values for $R_{p\star}/a$, Ω/Ω_c, and $\sin i_*$; and we have the ancillary observational quantities $P_{\rm orb}$ and $v_e \sin i_*$ to good accuracy.

In the Roche model, the critical angular rotation rate at which the equatorial surface gravity is zero is

$$\Omega_c = \sqrt{\frac{8}{27}\frac{GM_*}{R_{p*}^3}}.$$

The equatorial rotation speed is

$$\begin{aligned} v_e &= \Omega R_e = (\Omega/\Omega_c)\,\Omega_c\, f R_{p*} \\ &= f\left(\frac{\Omega}{\Omega_c}\right)\sqrt{\frac{8}{27}\frac{GM_*}{R_{p*}}}, \end{aligned} \tag{A1}$$

where again in the Roche model, the function f is given by

$$f = \frac{R_e}{R_{p*}} = \frac{3}{(\Omega/\Omega_c)}\cos\left[\frac{\pi + \cos^{-1}(\Omega/\Omega_c)}{3}\right]$$

(Harrington & Collins 1968). Using Kepler's third law,

$$\begin{aligned} M_* + M_P &\equiv M_*(1+q) \\ &= \frac{4\pi^2}{G\,P_{\rm orb}^2}\frac{R_{p*}^3}{(R_{p*}/a)^3}, \end{aligned}$$

for the mass in equation (A1), and rearranging, gives the semi-major axis:

$$a = \frac{P_{\rm orb}}{f\,(\Omega/\Omega_c)}\frac{v_e \sin i_*}{\sin i_*}\sqrt{\left(\frac{R_{p*}}{a}\right)\frac{27\,(1+q)}{32\pi^2}}. \tag{A2}$$

All terms on the right-hand side are 'known', except the mass ratio $q = M_P/M_*$, which it may often be reasonable to assume to be negligibly small if no numerical estimate is available. Having evaluated the orbital semi-major axis, the linear dimensions of the system components, and the mass, follow (radii from R/a, and M_* from Kepler's third law).

Using similar reasoning as above, we also have

$$\begin{aligned} P_{\rm rot} &= \frac{2\pi}{\Omega} \\ &= \frac{2\pi}{(\Omega/\Omega_c)}\sqrt{\frac{27}{8}\frac{R_{p*}^3}{GM_*}} \\ &= \frac{P_{\rm orb}}{(\Omega/\Omega_c)}\sqrt{\left(\frac{3}{2}\frac{R_{p*}}{a}\right)^3(1+q)}. \end{aligned} \tag{A3}$$

Thus in the Roche model the rotation period (or, equivalently, Ω) is scale-free, and of itself offers no independent leverage on absolute values of M_* or $R_{p\star}$. However, if $P_{\rm rot}$ is known from independent considerations, it may be used to constrain the combination $(R_{p\star}/a)^{3/2}(\Omega/\Omega_c)^{-1}$ (Section 5.3).

This paper has been typeset from a TEX/LATEX file prepared by the author.